

A Li *K*-edge XANES study of salts and minerals

Cedrick O'Shaughnessy,^{a*} Grant S. Henderson,^a Benjamin J. A. Moulton,^{a,b}
Lucia Zuin^c and Daniel R. Neuville^d

^aDepartment of Earth Sciences, University of Toronto, Canada, ^bDepartamento de Física, Universidade Federal de São Carlos, Brazil, ^cCanadian Light Source Inc., University of Saskatchewan, Canada, and ^dLaboratoire des Géomatériaux, CNRS – Institut de Physique du Globe de Paris, France. *Correspondence e-mail: c.oshaughnessy@mail.utoronto.ca

Received 17 July 2017

Accepted 15 January 2018

Edited by A. F. Craievich, University of São Paulo, Brazil

Keywords: XANES; lithium; silicates; phosphates; salts.

The first comprehensive Li *K*-edge XANES study of a varied suite of Li-bearing minerals is presented. Drastic changes in the bonding environment for lithium are demonstrated and this can be monitored using the position and intensity of the main Li *K*-absorption edge. The complex silicates confirm the assignment of the absorption edge to be a convolution of triply degenerate *p*-like states as previously proposed for simple lithium compounds. The Li *K*-edge position depends on the electronegativity of the element to which it is bound. The intensity of the first peak varies depending on the existence of a *2p* electron and can be used to evaluate the degree of ionicity of the bond. The presence of a *2p* electron results in a weak first-peak intensity. The maximum intensity of the absorption edge shifts to lower energy with increasing SiO₂ content for the lithium aluminosilicate minerals. The bond length distortion of the lithium aluminosilicates decreases with increasing SiO₂ content, thus increased distortion leads to an increase in edge energy which measures lithium's electron affinity.

1. Introduction

Lithium is the lightest alkali metal, but also one of the fastest diffusing elements in silicates (Jambon & Semet, 1978). Lithium isotopes in the outer layers of the Earth (hydrosphere, crust and lithospheric mantle) can be fractionated by up to 60% (Tomascak, 2004). The structural chemistry of lithium-bearing minerals is of particular interest because of the implications with respect to economic geology. Granitic pegmatite deposits contain lithium in a variety of exotic minerals which have diverse bonding environments (London, 2005). The main industrial use for lithium is in sacrificial anodes in batteries and the inorganic compounds which form on the surface of these anodes have motivated many studies (Kobayashi *et al.*, 2007; Lu *et al.*, 2011; Ogasawara *et al.*, 2015; Wang & Zuin, 2017). There is difficulty in understanding the structure of lithium in different crystals because it is nearly invisible to X-ray diffraction (XRD) and the possibility of paraelectric behaviour in these compounds. The use of X-ray absorption near-edge structure (XANES) spectroscopy presents us with an alternative method of probing this structure. We have examined the Li *K*-edge of a variety of synthetic Li-bearing compounds as well as a suite of natural minerals from around the world (Table 1). We hope these results will be useful as a fingerprinting method for amorphous lithium materials (lithium silicate glasses, glass ceramics or melts), as well as aiding in identification of unknown compounds and highly irregular lithium bonding environments.

XANES is a synchrotron-based technique which can provide information on the electronic, magnetic and structural

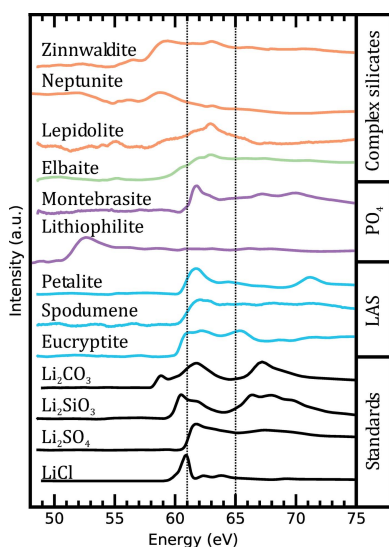


Table 1
Symmetry, coordination number (CN) and mean bond length ($\langle\text{Li}-X\rangle$).

Mineral	Formula	Symmetry		CN	$\langle\text{Li}-X\rangle$ (Å) [†]	Locality
Li chloride	LiCl	Isometric	$Fm\bar{3}m$	6	2.57 ^[1]	Synthetic
Li sulfate	Li ₂ SO ₄	Monoclinic	$P2_1/c$	4	1.97 ^[2]	Synthetic
Li carbonate	Li ₂ CO ₃	Monoclinic	$C2/c$	4	1.97 ^[3]	Synthetic
Li metasilicate	Li ₂ SiO ₃	Orthorhombic	$Cmc2_1$	4	2.00 ^[4]	Synthetic
Eucryptite	LiAlSiO ₄	Trigonal	$R\bar{3}$	4	1.99 ^[5]	Bikita, Zimbabwe
Spodumene	LiAlSi ₂ O ₆	Monoclinic	$C2/c$	6	2.21 ^[6]	Minas Gerais, Brazil
Petalite	LiAlSi ₄ O ₁₀	Monoclinic	$P2/c$	4	1.94 ^[7]	Minas Gerais, Brazil
Montebrasite	LiAl(PO ₄)(OH)	Triclinic	$P\bar{1}$	6	2.11 ^[8]	Montebras, France
Lithiophilite	LiMn ²⁺ PO ₄	Orthorhombic	Pmn	6	2.16 ^[9]	Branchville, USA
Elbaite	Na(Li,Al) ₃ Al ₆ (Si ₆ O ₁₈)(BO ₃)(OH) ₃ (OH)	Trigonal	$R3m$	6	2.02 ^[10]	California, USA
Lepidolite	KLi ₂ Al·(Si ₄ O ₁₀)(F,OH) ₂	Monoclinic	$C2/c$	6	2.12 ^[11]	Minas Gerais, Brazil
Zinnwaldite	KLiFe ²⁺ Al(AlSi ₃ O ₁₀)(F,OH) ₂	Monoclinic	$C2$	6	1.89 ^[12]	Zinnwald, Germany
Neptunite	LiNa ₂ K(Fe ²⁺ ,Mn ²⁺) ₂ Ti ₂ (Si ₈ O ₂₄)	Monoclinic	Cc	6	2.11 ^[13]	San Benito, USA

[†] References: [1] Wyckoff (1963). [2] Albright (1933). [3] Zemann (1957). [4] Hesse (1977). [5] Daniels & Fyfe (2001). [6] Clark *et al.* (1968). [7] Ross *et al.* (2015). [8] Groat *et al.* (2003). [9] Hatert *et al.* (2012). [10] Gatta *et al.* (2012). [11] Sartori *et al.* (1973). [12] Guggenheim & Bailey (1977). [13] Cannilo *et al.* (1966).

properties of matter (Henderson *et al.*, 2014). It is a process in which a photon of light excites a core electron to an unoccupied molecular orbital state. The photon must have an energy which is larger than or equal to that of the binding energy of the electron. The binding energy of the electron is different for every element, which is why XANES is an element-specific technique which can be tuned to investigate any element of interest. When the electron is excited to a higher empty state, a photon is emitted as the core hole is filled and this fluorescence may be measured to yield the absorption spectrum (FLY).

The Li *K*-edge is located between 55 and 65 eV depending on the environment of Li in the specific compound. Due to its very low energy, it is difficult to probe the Li *K*-edge, but over the last 15 years there has been an increase in the amount of work being performed using XANES, electron-energy-loss spectroscopy (EELS) and X-ray Raman scattering (XRS) (Tsuji *et al.*, 2002; Kobayashi *et al.*, 2007; Lu *et al.*, 2011; Fister *et al.*, 2011; Lee *et al.*, 2014; Pascal *et al.*, 2014; Kikkawa *et al.*, 2014; Taguchi *et al.*, 2015; Ogasawara *et al.*, 2015). Additionally, there has been a small body of computational work using density-functional theory (DFT) and molecular dynamics (MD) simulations on a number of different Li-bearing compounds (Jiang & Spence, 2004; Mauchamp *et al.*, 2006, 2008; Olovsson *et al.*, 2009a,b; Yiu *et al.*, 2013; Pascal *et al.*, 2014).

2. Methods

2.1. Mineral samples

A suite of nine mineral samples were collected from the Université Pierre-Marie Curie (UPMC), Paris, France (Table 1). The minerals were identified using Raman spectroscopy fingerprinting from the RRUFF database (Lafuente *et al.*, 2015). Additionally, four synthetic Li-bearing compounds were used as standards. The mineral samples were broken down to ~25 mm² chips appropriate for XANES experiments. The lithium metasilicate is a synthetic lithium silicate (LS) glass sample which was recrystallized whereas the

lithium sulfate, carbonate and chloride are all high-quality powders (>99%). All samples were kept in a desiccator before being transferred to the experimental chamber (detailed in §2.2).

2.2. XANES spectroscopy

The Li *K*-edge XANES measurements were performed at the Canadian Light Source Inc. (CLS), Saskatoon, Canada, at the variable-line-spacing plane-grating monochromator (VLS-PGM) beamline (Hu *et al.*, 2007). The spectra were collected in fluorescence yield (FLY) and total electron yield (TEY) (Wang & Zuin, 2017). Many researchers have used FLY data because it is known to sample a larger volume of space which renders it more sensitive to bulk than TEY (Kasrai *et al.*, 1993; Jiang & Spence, 2006; Henderson *et al.*, 2014; Moulton *et al.*, 2016; Wang & Zuin, 2017). The penetration depth of the X-rays was calculated for Li₂CO₃ as 75–95 nm using FLY compared with 1 nm for TEY by Wang & Zuin (2017) in their Fig. S1. Additionally, the resolution of the FLY spectra was considerably better than the TEY, which is why only the FLY spectra are reported in this paper. The geometry of the incident beam with respect to the microchannel plate detector is 90° with the sample at 45° to the incident beam in order to negate self-absorption effects (Kasrai *et al.*, 1993). The spectra were collected in the range 35–75 eV; some minerals also contain Mn, Fe and Al which cause overlap with the Mn *M*_{2,3}-edge (~47 eV), Fe *M*_{2,3}-edge (~53 eV) and Al *L*_{2,3}-edge (~73 eV). This is discussed on a sample-by-sample basis. The beamline slits were opened to 50 mm × 50 mm with a resolution $E/\Delta E > 10000$, and the pressure in the experimental chamber is maintained below 10⁻⁷ torr for all measurements (Wang & Zuin, 2017).

The Li *K*-edge spectra were processed by the following routine: (i) the fluorescence signal was intensity normalized to the incoming intensity (*I*₀), measured by a Ni mesh located upstream of the sample chamber; (ii) a two-step polynomial background subtraction was performed on the pre-edge region (~35–58 eV) and post-edge region (~65–75 eV) following the edge processing of Moulton *et al.* (2016); (iii) the resulting spectra were then intensity normalized setting the

maximum intensity peak to a value of 1. After the normalization procedure, the final spectra of the Li-bearing salt standards (LiCl, Li₂CO₃ and Li₂SO₄) were compared with previously published experimental spectra and were in accord (Tsuji *et al.*, 2002; Handa *et al.*, 2005; Fister *et al.*, 2011; Pascal *et al.*, 2014). Finally, the edge value of our lithium chloride (LiCl) sample has been calibrated to the edge value of 60.8 eV (Tsuji *et al.*, 2002), following the procedure of Wang & Zuin (2017), and the remaining spectra have all been shifted by an equal amount. The calibrated positions are the same as the edge positions obtained in previous XANES (Tsuji *et al.*, 2002; Handa *et al.*, 2005) and XRS (Fister *et al.*, 2011; Pascal *et al.*, 2014) studies with a maximum edge difference of ±0.1 eV.

3. Results

The results are divided into sections according to the similarities the spectra have with one another. We begin with the four salt standards (LiCl, Li₂SO₄, Li₂SiO₃, Li₂CO₃), followed by the lithium aluminosilicate minerals (eucryptite, spodumene and petalite), complex silicates (elbaite and phyllosilicates: lepidolite, neptunite and zinnwaldite) and finally the lithium phosphates (lithiophilite and montebrasite). For comparison, all the spectra are shown in Fig. 1 and their peak positions are compiled in Table 2.

3.1. Lithium salts and metasilicate

3.1.1. Lithium chloride (LiCl). The first standard to be considered is lithium chloride which is isometric (*Fm3m*) with Li ions occupying the Na site in the halite structure. The Na *K*-edge of halite (NaCl) has previously been investigated using a combination of XANES and *ab initio* calculations and displays a number of complex features which have been attributed to the high symmetry of the close-packed B1 structure type (Kasrai *et al.*, 1991; Kikas *et al.*, 2001; Prado & Flank, 2005; Neuvillie *et al.*, 2004). The Li *K*-edge absorption spectrum consists of a sharp main peak (peak *A*) at 60.8 eV similar to that observed in the Na *K*-edge of halite. The two spectra differ due to a small number of additional features present in the spectrum of LiCl which has a low-intensity doublet located at 62.4 eV (peak *C*) and 63.8 eV (peak *E*) (Fig. 2). Additionally, peak *A* is asymmetric on the low-energy side and undergoes a change in slope between 59.5 and 60.4 eV; this pre-edge feature will be referred to as peak *p*. The spectrum of LiCl shows all the same features as those presented in previous XANES studies on lithium halides (Handa *et al.*, 2005; Wang & Zuin, 2017).

3.1.2. Lithium sulfate (Li₂SO₄). Lithium sulfate is an ionic compound with monoclinic symmetry (*P2₁/c*), with Li atoms surrounded by four oxygen atoms which belong to a sulfate

Table 2
Peak positions in lithium-bearing salts and minerals.

Peak positions are precise to ±0.05 eV.

Mineral	<i>p</i> '	<i>p</i>	<i>A</i>	<i>B</i>	<i>C</i>	<i>D</i>	<i>E</i>	<i>F</i>	<i>G</i>	<i>H</i>
Li chloride	–	59.5	60.8	–	62.4	–	63.8	–	–	69.3
Li sulfate	–	59.0	–	61.7	–	63.0	64.0	–	67.1	69.1
Li metasilicate	–	–	60.5	61.8	–	–	–	66.4	68.0	69.6
Li carbonate	–	58.8	–	61.8	–	–	–	–	67.2	69.2
Eucryptite	57.2	–	61.2	–	62.2	63.1	–	65.3	68.7	–
Spodumene	56.5	58.7	–	–	62.1	62.7	64.3	65.8	68.2	–
Petalite	57.6	–	–	61.7	–	–	64.4	–	67.3	–
Montebrasite	–	–	60.8	61.8	–	62.8	64.9	–	67.2	–
Lithiophilite	–	–	60.9	61.8	–	63.0	–	66.1	67.9	–
Elbaite	–	–	60.4	–	62.1	63.0	–	65.7	67.3	–
Lepidolite	–	59.3	–	61.6	–	62.9	–	65.6	67.7	–
Zinnwaldite	–	–	–	–	–	63.0	–	66.1	68.1	–
Neptunite	–	–	–	–	–	63.1	–	65.6	–	–

group (Albright, 1933). The spectrum of Li₂SO₄ comprises a main absorption edge located at 61.72 eV (peak *B*) and a secondary broad peak with two features at 67.0 eV (peak *G*) and 69.1 eV (peak *H*) (Fig. 2). Peak *B* is also characterized by a small pre-edge feature at 59 eV (peak *p*) and a shoulder composed of a doublet similar to that found in the spectrum of LiCl at 63.0 eV (peak *D*) and 64.0 eV (peak *E*). The energy of all the features are in agreement with the XRS and *ab initio*

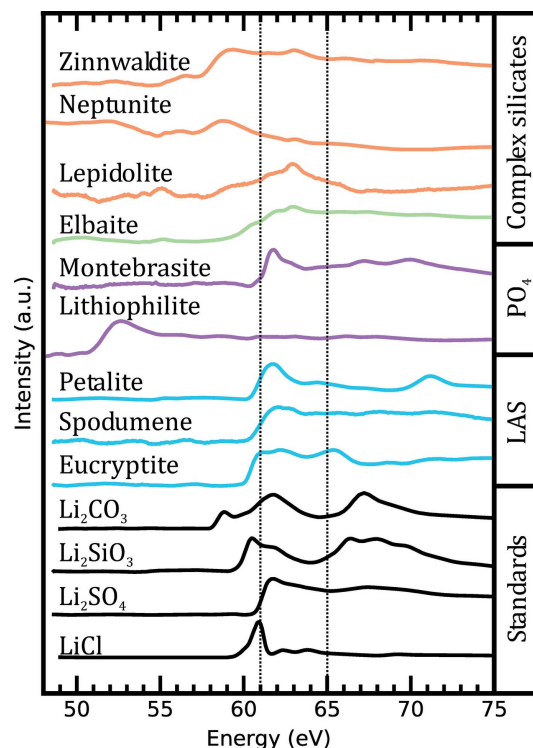


Figure 1
Li *K*-edge spectra of our sample suite. The standards (black), the LAS minerals (blue) with increasing SiO₂ content, the phosphate minerals (pink), tourmaline (green) and the phyllosilicates (orange) are maximal intensity normalized. The dotted lines are located at 61 eV and 65 eV and serve as a guide for the eyes when comparing the different spectra (same locations for all figures). Note that the proximity of the Fe *M*_{2,3}-edge and Mn *M*_{2,3}-edge to the Li *K*-edge creates overlapping edge contributions and these complications are discussed in the text.

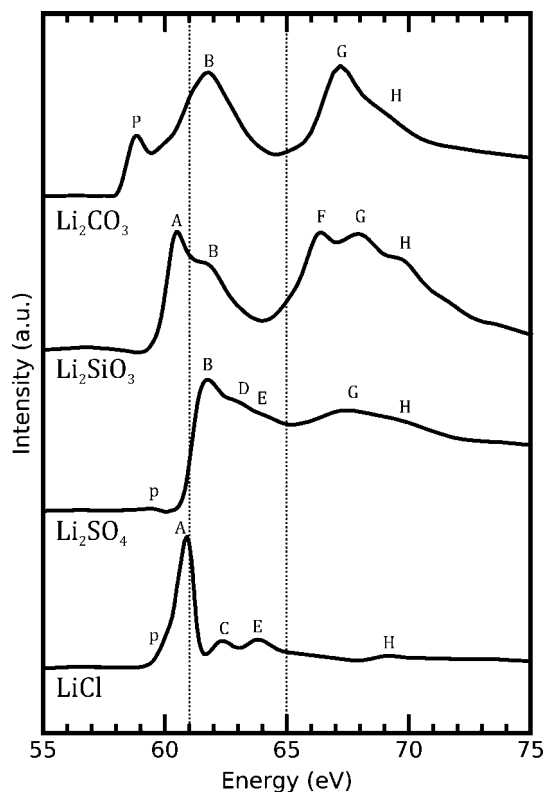


Figure 2
Li *K*-edge spectra of standard compounds used to calibrate and interpret the results for the mineral suite. Note the sharp absorption edge in LiCl, Li₂SO₄ and Li₂SiO₃ and how it contrasts with the lower energy pre-edge (peak *p*) observed in Li₂CO₃.

molecular dynamics (AIMD) simulations of Pascal *et al.* (2014).

3.1.3. Lithium metasilicate (Li₂SiO₃). Lithium metasilicate has orthorhombic symmetry (*Cmc*₂₁) and is composed of parallel chains of SiO₄ tetrahedra in the [001] direction (Hesse, 1977). Lithium is tetrahedrally coordinated and has a mean Li–O distance of 2.00 Å (Hesse, 1977). The spectrum of lithium metasilicate exhibits two main features: (i) the main absorption edge at 60.5 eV (peak *A*) with a shoulder at 61.8 eV (peak *B*); and (ii) a triplet at 66.4 (peak *F*), 68.0 (peak *G*) and 69.6 eV (peak *H*) (Fig. 2). As is the case with the remaining spectra to be presented in the study, there are no previous XANES Li *K*-edge data available for comparison.

3.1.4. Lithium carbonate (Li₂CO₃). Lithium carbonate is monoclinic (*C2/c*) with Li in tetrahedral coordination (Zemann, 1957). The XANES spectrum of lithium carbonate differs quite drastically from that of both LiCl and Li₂SO₄ due to its very strong pre-edge feature located at 58.8 eV (peak *p*) (Fig. 2). The main edge is found at 61.8 eV (peak *B*) and appears to be the product of three contributions as the peak shows inflection points at both the low- and high-energy sides of the maximum intensity. The second broad feature is located at ~67 eV and seems to be composed of at least two contributions at 67.2 eV (peak *G*) and 69.2 eV (peak *H*). The features in the experimental spectrum are in agreement with those of Pascal *et al.* (2014) though their result does not

resolve peak *p*. Conversely, their simulations predict this pre-edge feature in both the results for the AIMD simulations at 298 K and the excited electron and core-hole (XCH) formalism of DFT for a static crystal at 0 K (Pascal *et al.*, 2014). It appears that XANES is better suited than XRS at resolving higher-resolution features in the Li *K*-edge.

3.2. Lithium aluminosilicates minerals (LAS)

A series of three aluminosilicates was analyzed in order to evaluate the effect of increasing SiO₂ concentration on the absorption edge of lithium. The lithium aluminosilicates are eucryptite (LiAlSiO₄), spodumene (LiAlSi₂O₆) and petalite (LiAlSi₄O₁₀) and their silica concentration increases in that order. These three phases fall along the tie-line between SiO₂ and Li₂O·Al₂O₃ in the Li₂O–Al₂O₃–SiO₂ phase diagram (Roy & Osborn, 1949, Fig. 1). It is worth noting that eucryptite and spodumene are two very important phases for glass ceramics, particularly for Zerodur low-expansion glass ceramics. The samples show systematic trends in edge energy with changing composition elaborated below (Fig. 3). It is important to note that due to the aluminium content the data at energies greater than 70 eV are subject to interference due to the presence of the Al *L*_{2,3}-absorption edge which is located around 72 eV.

3.2.1. Eucryptite (LiAlSiO₄). α-Eucryptite has *R* $\bar{3}$ symmetry and consists of three symmetrically non-equivalent tetrahedral sites with one site occupied solely by Li and the other two

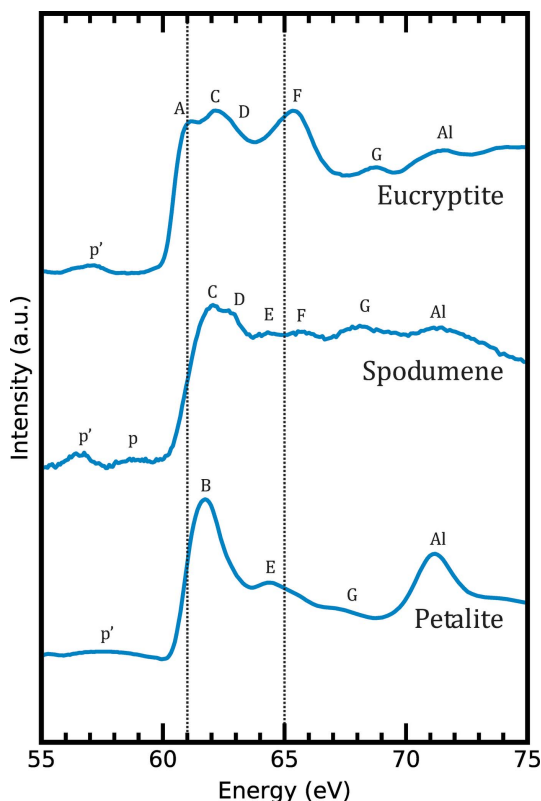


Figure 3
Li *K*-edge spectra of lithium aluminosilicate minerals. The samples have three peaks contributing to the main edge (*A*, *B* and *C*) with both peaks *A* and *C* visible in eucryptite.

being partly occupied by both Si and Al (Hesse, 1985; Daniels & Fyfe, 2001). Hesse (1985) described α -eucryptite as being isostructural to willemite (Zn_2SiO_4). All three types of tetrahedra (Li, Al and Si) are connected to eight other tetrahedra *via* bridging oxygen atoms (which are all threefold coordinated) and form channels along [0001] with six-membered rings perpendicular to the channels (Daniels & Fyfe, 2001, Fig. 2).

The Li *K*-edge spectrum of α -eucryptite displays a main absorption edge which is split into a doublet at 61.2 eV (peak A) and 62.2 eV (peak C) with the latter having higher intensity and a small shoulder (peak D) (Fig. 3). There is a pre-edge feature located at 57.2 eV (peak *p'*) and another major feature at 65.3 eV (peak F). There are two smaller peaks at 68.7 eV (peak G) and 71.5 eV (due to the Al $L_{2,3}$ -edge).

3.2.2. Spodumene ($\text{LiAlSi}_2\text{O}_6$). Spodumene is a *c*-centered clinopyroxene which occurs in three different modifications which depend on temperature (Li & Peacor, 1968; Arlt & Angel, 2000). α -Spodumene (monoclinic, $C2/c$) is the only naturally occurring room-temperature phase while β -spodumene (tetragonal) and γ -spodumene (hexagonal, highly packed and related to β -quartz) are high-temperature polymorphs (Li & Peacor, 1968). The spodumene sample used in these experiments is the room-temperature α -spodumene phase. The lithium atoms are located in the octahedral *M2* site where other atoms such as Na and Ca may also be located depending on the sample (Clark *et al.*, 1968).

The spectrum of spodumene is also composed of a main absorption edge consisting of a doublet located at 62.1 eV (peak C) and 62.7 eV (peak D), respectively. Once again there is the presence of a pre-edge feature, but in the form of a doublet at 56.5 eV (peak *p'*) and 58.7 eV (peak *p*) (Fig. 3). The higher-energy portion of the spectrum may be divided into three parts, this appears similar to eucryptite: (i) a low-intensity doublet at 64.3 eV (peak E) and 65.8 eV (peak F); (ii) a narrow asymmetrical peak at 68.2 eV (peak G); and (iii) a broad peak at 71.2 eV (Al $L_{2,3}$ -edge).

3.2.3. Petalite ($\text{LiAlSi}_4\text{O}_{10}$). Petalite is a monoclinic mineral with space group $P2/c$ (Liebau, 1961). It occurs as α -petalite at ambient pressure and undergoes a phase transition at 2.71 GPa to form β -petalite. This transition is isomorphic and results in the tripling of the unit-cell volume (Ross *et al.*, 2015). Petalite consists of sheets of corner-sharing SiO_4 tetrahedra which are connected to one another *via* AlO_4 tetrahedra (Liebau, 1961; Ross *et al.*, 2015). The lithium atoms are also found in four-coordinate polyhedra and their geometry varies between square planar and a typical tetrahedron (Ross *et al.*, 2015).

The absorption spectrum of petalite differs from both that of eucryptite and spodumene due to the main edge being composed of one single peak located at 61.7 eV (peak B) though it has a shoulder on the high-energy side (Fig. 3). There is also a pre-edge feature for petalite, though it is much broader than that found in eucryptite. It is found at 57.6 eV (peak *p'*) and may be similar to the doublet observed in spodumene but with both peaks overlapping making them indistinguishable. Furthermore, we observe similar features in

the region between 63 and 73 eV as we did for both eucryptite and spodumene. This region is composed of two peaks at 64.4 eV (peak E) and 67.3 eV (peak G) as well as a third more pronounced peak located at 71.0 eV (Al $L_{2,3}$ -edge).

3.3. Lithium phosphates (PO_4)

Lithium-bearing phosphate minerals, specifically those which contain Fe, Mn and Co, have been proposed as alternative materials to LiCoO_2 for use as a cathode in lithium-ion batteries (Yiu *et al.*, 2013, and references therein).

3.3.1. Montebbrasite [$\text{LiAl}(\text{PO}_4)(\text{OH})$]. The structure of montebbrasite is triclinic ($P\bar{1}$) (Baur, 1959; Groat *et al.*, 2003). It often displays solid solution with amblygonite [$\text{LiAl}(\text{PO}_4)(\text{F})$]. Aluminium octahedra form corner-sharing chains along the *c*-axis which are cross-linked by tetrahedral phosphates forming a tetrahedral–octahedral network (Groat *et al.*, 2003). Lithium sits in a sixfold-coordinated site in pure montebbrasite but if F is added to the structure it causes site disorder between Li in proximity of OH *versus* F and the occupancy is more accurately described by using a split Li site model (Groat *et al.*, 2003).

The spectrum of montebbrasite displays a sharp absorption edge at 61.8 eV (peak B) with two shoulder features at 60.8 eV (peak A) and 62.8 eV (peak D) (Fig. 4). Further from the edge lie three features: (i) a shallow peak at 64.9 eV (peak E); and

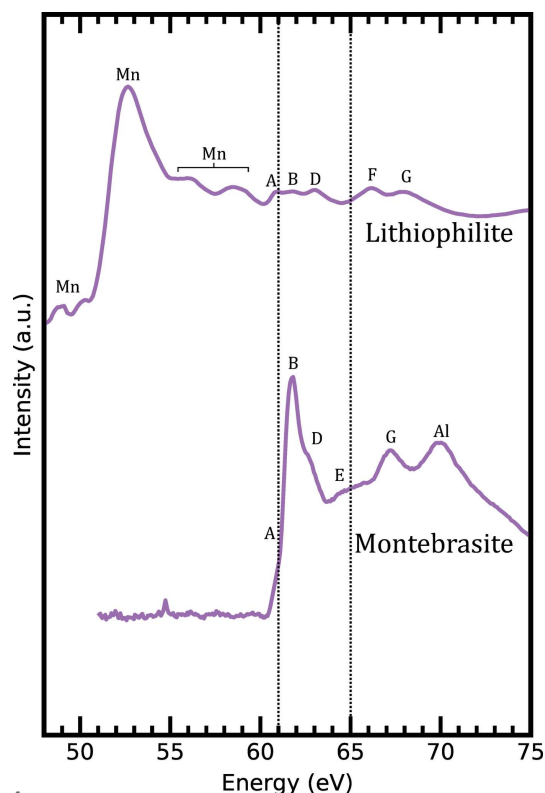


Figure 4

Li *K*-edge spectra of phosphate minerals. Montebbrasite demonstrates a well defined, sharp absorption edge as was the case with our standards as well as petalite. Lithiophilite conversely is difficult to interpret due to the overlap of the Mn $M_{2,3}$ -edge which is labeled above. Nevertheless, several features from lithiophilite have similar energies to those observed in montebbrasite.

(ii) a well defined doublet at 67.2 eV (peak *G*) and 70.0 eV (Al $L_{2,3}$ -edge). The spectral features of montebrasite were used to aid the peak assignments for lithiophilite which are more difficult due to the overlapping Mn $M_{2,3}$ -edge (Fig. 4).

3.3.2. Lithiophilite ($\text{LiMn}^{2+}\text{PO}_4$). The second phosphate of interest is lithiophilite ($\text{LiMn}^{2+}\text{PO}_4$), an orthorhombic mineral (*Pmnb*) which is isostructural to olivine Mg_2SiO_4 (Geller & Durand, 1960). Lithium and manganese are both located in octahedral sites which are highly distorted whereas the phosphorous is found in discrete tetrahedra (PO_4) (Geller & Durand, 1960). The *M1* (Li and vacancies) and *M2* (Mn) octahedra form two distinct types of chains throughout the structure (Hatert *et al.*, 2012).

We observe significant contributions from the Mn $M_{2,3}$ -edge in the spectrum of lithiophilite akin to neptunite (see below, Fig. 4). Using the information obtained from montebrasite we have isolated the peaks which are caused by the Li *K*-edge of lithiophilite. The main absorption edge is composed of a triplet at 60.9 eV (peak *A*), 61.8 eV (peak *B*) and 63.0 eV (peak *D*). Similarly to montebrasite we also observe a well defined doublet at 66.1 eV (peak *F*) and 67.9 eV (peak *G*).

3.4. Complex lithium-bearing silicates: phyllosilicates and cyclosilicates

We now consider more complex lithium silicates which provide very different bonding environments for lithium to those mentioned above (Fig. 5). This suite consists of a cyclosilicate in the form of the tourmaline end-member elbaite, as well as three phyllosilicates (lepidolite, zinnwaldite and neptunite).

3.4.1. Elbaite [$\text{Na}(\text{Li},\text{Al})_3\text{Al}_6(\text{Si}_6\text{O}_{18})(\text{BO}_3)(\text{OH})_3(\text{OH})$]. The tourmaline group of minerals are structurally complex borocyclosilicates [$\text{XY}_3\text{Z}_6(\text{T}_6\text{O}_{18})(\text{BO}_3)_3\text{V}_3\text{W}$, where *X* = Ca, Na, K; *Y* = Al, Fe^{2+} , Fe^{3+} , Li, Mg, Mn; *Z* = Al, Cr^{3+} , Fe^{3+} , V^{3+} ; *T* = Si, Al, B; *V* = O, OH; *W* = F, O, OH] and are found in a wide range of natural environments (Hawthorne & Henrys, 1999; Gatta *et al.*, 2012). We are specifically interested in the elbaite end-member as it is the sodium-rich Li-bearing tourmaline member (Donnay & Barton, 1972). It has a trigonal crystal structure with space group *R3m* and lithium is found in an octahedral site (ZO_6) shared with aluminium (Gatta *et al.*, 2012). This octahedral site along with an Al-specific octahedral site (YO_6) link the six-membered rings of tetrahedra (TO_4 , *T* = Si, Al and B) to the triangular BO_3 site (Gatta *et al.*, 2012).

Considering the complexity of elbaite, one cannot be surprised by the number of features and shape of its XANES spectrum (Fig. 5). The main edge is located at 63.0 eV (peak *D*) and has two features at slightly lower energy. The first is an apparent change in slope occurring at 60.4 eV (peak *A*) and the second is a shoulder appearing at 62.1 eV (peak *C*). Similar to the spectra of the lithium aluminosilicates, the spectrum of elbaite consists of three smaller features at higher energies: 65.7 eV (peak *F*), 67.3 eV (peak *G*) and 70.9 eV (Al $L_{2,3}$ -edge).

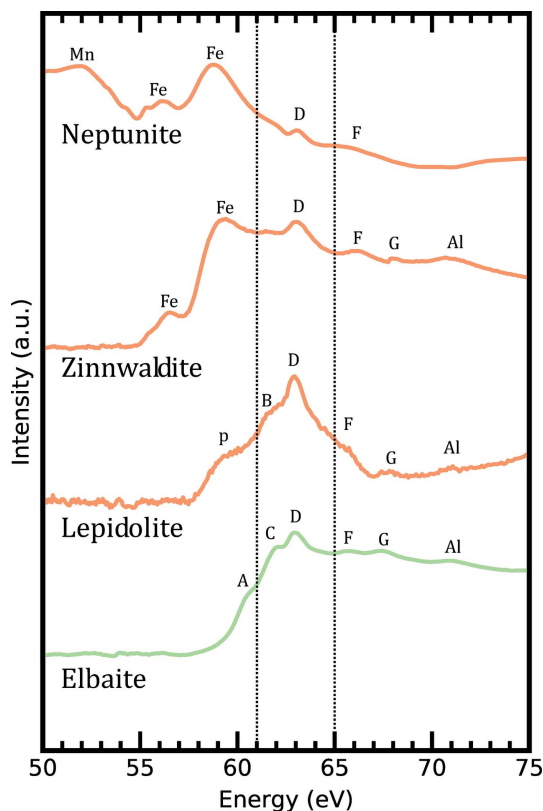


Figure 5

Li *K*-edge spectra of a Li-bearing tourmaline and three phyllosilicates. Elbaite displays a main peak (*D*) with two lower intensity pre-edge features. The main peak in lepidolite (*D*) resembles that of elbaite but is broader; they both are similar to Li_2CO_3 . Zinnwaldite has an Fe $M_{2,3}$ -edge contribution which renders the low-energy part of the spectrum difficult to interpret but has a main peak (*D*) position similar to that of lepidolite and elbaite. Neptunite has both an Fe $M_{2,3}$ -edge and a Mn $M_{2,3}$ -edge overlapping the low-energy portion but also has a main peak (*D*) located at a similar position to the aforementioned minerals.

3.4.2. Lepidolite [$\text{KLi}_2\text{Al}(\text{Si}_4\text{O}_{10})(\text{F},\text{OH})_2$]. Lepidolite [$\text{KLi}_2\text{Al}(\text{Si}_4\text{O}_{10})(\text{F},\text{OH})_2$] is monoclinic (*C2/c*) (Sartori *et al.*, 1973). There are three polytypes of lepidolite (*1M*, *2M₁* and *2M₂*) and they can be differentiated using techniques such as electron-backscattered diffraction (Guggenheim, 1981; Kogure & Bunno, 2004). Guggenheim (1981) described *1M* lepidolites of symmetry *C2/m* as having the potential of octahedral ordering between *M1* and two *M2* sites along a mirror plane. As outlined by Sartori *et al.* (1973), the features of *2M₂* polytype lepidolites to note are the remarkable octahedral ordering (one of these sites is almost exclusively occupied by Li), and the distortion of the tetrahedra which make up the tetrahedral sheets (resembling trigonal pyramids). For the purpose of this study, we are focusing our efforts on the more common *1M* polytype of lepidolite. Future work should be carried out on the different polytypes in order to differentiate them using Li *K*-edge XANES, similar to what has been achieved for aluminium and other elements (Mottana *et al.*, 2002).

Even though lepidolite is quite different from elbaite certain similarities are observed in both spectra (Fig. 5). The absorption edge is also composed of three contributions which

are located at 59.3 eV (peak *p*, shoulder), 61.6 eV (peak *B*, shoulder) and 62.9 eV (peak *D*, main peak). On the high-energy side of the main peak (*D*) we observe an inflection at 65.6 eV (peak *F*). The remaining portion of the spectrum is composed of two additional peaks located at 67.7 eV (peak *G*) and 71.0 eV (Al $L_{2,3}$ -edge).

3.4.3. Zinnwaldite [$\text{KLiFe}^{2+}\text{Al}(\text{AlSi}_3\text{O}_{10})(\text{F},\text{OH})_2$]. A tri-octahedral mica, zinnwaldite [$\text{KLiFe}^{2+}\text{Al}(\text{AlSi}_3\text{O}_{10})(\text{F},\text{OH})_2$] is monoclinic (*C2*) comparable with lepidolite (Guggenheim & Bailey, 1977). Lithium is found in the larger of two octahedral sites, shared with Fe^{2+} , Mg and Mn and their respective quantities vary depending on polytype and formation environment (Guggenheim & Bailey, 1977). As seen in lepidolite there are both *1M* and *2M* polytypes of zinnwaldite (Rieder, 1968).

The spectrum of zinnwaldite is difficult to interpret due to the overlap of the Fe $M_{2,3}$ -edge which is located at ~ 53 eV (Fig. 5). The first band observed at 59.3 eV (peak Fe) corresponds to the main absorption band of the Fe $M_{2,3}$ -edge (van der Laan, 1991; Garvie & Buseck, 2004). The first observable Li feature is the main absorption edge located at 63.0 eV (peak *D*). Analogous to lepidolite and elbaite we observe three contributions at higher energies; a well defined peak on the high-energy side of the main absorption band centered at 66.1 eV (peak *F*) followed by a small asymmetrical peak at 68.1 eV (peak *G*) and finally the typical broad peak at 70.8 eV (Al $L_{2,3}$ -edge).

3.4.4. Neptunite [$\text{LiNa}_2\text{K}(\text{Fe}^{2+},\text{Mn}^{2+})_2\text{Ti}_2(\text{Si}_8\text{O}_{24})$]. The final phyllosilicate is neptunite, a piezoelectric mineral with space group *Cc* and general formula $\text{LiNa}_2\text{K}(\text{Fe}^{2+},\text{Mn}^{2+})_2\text{Ti}_2(\text{Si}_8\text{O}_{24})$ (Cannilo *et al.*, 1966). The structure can be described as a cage made up of two 18-membered and four 14-membered rings of SiO_4 tetrahedra; this cage is then repeated *via* translation (Cannilo *et al.*, 1966). Though no previous XANES experiments have been conducted on the Li *K*-edge, the Ti *K*-edge of neptunite has previously been reported and correlated to both the coordination and size of the two Ti sites (Waychunas, 1987; Farges *et al.*, 1996).

The absorption spectrum of neptunite displays similar features as that of zinnwaldite due to the overlap of the Fe $M_{2,3}$ -edge but it is also complicated by the presence of the Mn $M_{2,3}$ -edge (Fig. 5). However, the contribution from the Li *K*-edge is still apparent with the main peak visible at 63.1 eV (peak *D*) as well as a broad feature located at 65.6 eV (peak *F*).

4. Discussion

4.1. Compositional effects on the bonding of lithium

The lithium-bearing standards provide an opportunity to understand features observed in the Li *K*-edge spectra of more complex mineral standards. They also have the added benefit of having been previously investigated using a variety of experimental (XANES and XRS) and theoretical (DFT and AIMD) techniques (Tsuji *et al.*, 2002; Handa *et al.*, 2005; Fister *et al.*, 2011; Pascal *et al.*, 2014; Wang & Zuin, 2017).

The combined XANES and discrete variational $X\alpha$ molecular orbital (DV- $X\alpha$) simulations of Tsuji *et al.* (2002) showed a correlation between the existence of the $2p$ electron and the shape of the core exciton peak. In compounds such as Li metal, Li_2O , Li_2CO_3 and Li_2S , a $2p$ electron exists at the exciton level because the ionic bond is weak (Tsuji *et al.*, 2002). This is manifested as a significant pre-edge feature in the spectra rather than a sharp absorption edge as seen in the lithium halides (Tsuji *et al.*, 2002; Handa *et al.*, 2005).

Furthermore, a Li *K*-edge XANES study of lithium halides by Handa *et al.* (2005) demonstrated that the edge position was sensitive to the type of halide bound to lithium; they noted a positive shift in the edge energy with increasing halide electronegativity. We compared the position of the first sharp peak of lithium metasilicate, montebasite and lithium sulfate to see the influence of the next nearest neighbour (Si, P and S, respectively). The shift in the edge position increases with the increasing electronegativity of the next nearest neighbour which is the same trend observed in the lithium halides (Handa *et al.*, 2005).

More recently, similar results on lithium compounds with weak ionic bonds (*e.g.* Li_2O , LiOH and Li_2CO_3) have been obtained using XRS and band-structure calculations carried out using the Bethe–Salpeter equation (BSE) under DFT (Fister *et al.*, 2011). The authors observed an overlap between the *s*- and *p*-DOS features in all the compounds they studied which points to *s*–*p* hybridization and can also be used to separate the symmetry of discrete features (Fister *et al.*, 2011). In the case of Li_2CO_3 they showed a clear correlation between the pre-edge feature in the Li *K*-edge spectrum and the same feature in the C *K*-edge which is typically associated with the π^* orbital in carbonate anions (Fister *et al.*, 2011). Furthermore, Pascal *et al.* (2014) demonstrated that in both LiF and Li_2SO_4 the strong absorption peak was due to triply degenerate *p*-like states which are separated by ~ 1 eV.

4.2. Bond length distortion in lithium aluminosilicate minerals

The lithium aluminosilicates provide the possibility of investigating the effect of the $\text{Li}_2\text{O}:\text{SiO}_2$ ratio along a compositional tie-line. The position (x_c) of the edge feature with the highest intensity (peaks *A*, *B*, or *C*) was compared with the $\text{Li}_2\text{O}:\text{SiO}_2$ ratio and demonstrates that at higher Li_2O content the position of the first peak is located at higher energy [Fig. 6(a)]. The position reflects the strength of the Li–O bond which proves to be stronger with higher Li_2O content. The bond strength is typically related to the distortion of the Li polyhedron (*i.e.* the local environment).

Wenger & Armbruster (1991) investigated the oxygen coordination of Li in a large dataset of lithium minerals and compounds. In doing so, they determined the mean bond lengths (Li–O) for both tetrahedral (1.96 Å) and octahedral (2.15 Å) lithium (Wenger & Armbruster, 1991). Furthermore, they defined the bond-length distortion (BLD) as

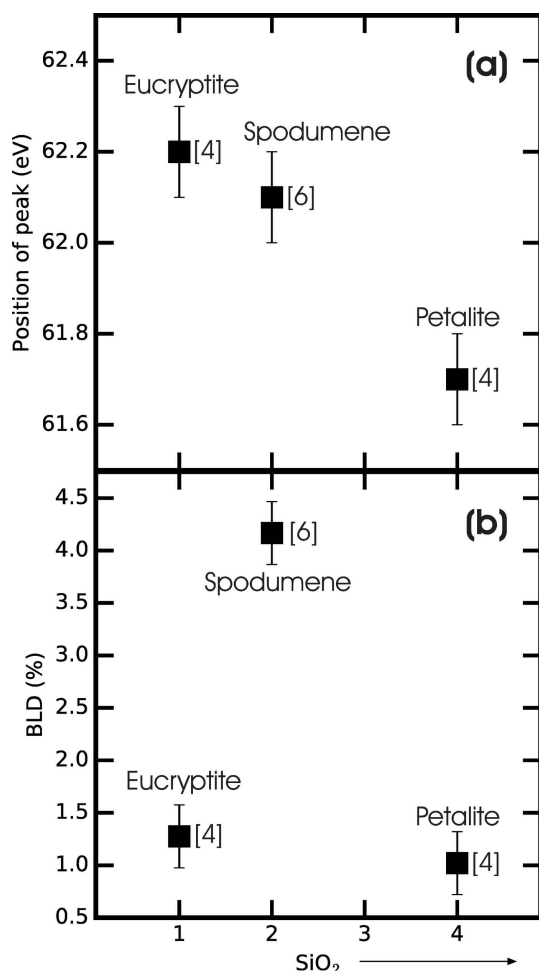


Figure 6

(a) The peak position is the location of the maximal peak intensity within the absorption edge triplet (observed in the LAS minerals). The minerals are plotted against SiO₂ (per formula unit) and are labeled above. Additionally, the coordination of lithium in the respective mineral is indicated (between brackets) as it is important to the calculation of the BLD. (b) The BLD was determined using the formula described by Wenger & Armbruster (1991) and their values for the mean bond lengths of four- and six-coordinated lithium minerals. The values for the individual bond lengths were obtained from Daniels & Fyfe (2001) (eucryptite), Clark *et al.* (1968) (spodumene) and Ross *et al.* (2015) (petalite).

$$\text{BLD} = \frac{100}{n} \sum_{i=1}^n \frac{|d_i - d_m|}{d_m} [\%], \quad (1)$$

where BLD is expressed as a percentage, n is the number of Li–O bonds, and d_i and d_m are the individual and mean Li–O bond lengths, respectively (Wenger & Armbruster, 1991). The calculated BLD was 1.28 for eucryptite (tetrahedral), 4.17 for spodumene (octahedral) and 1.02 for petalite (tetrahedral) [Fig. 6(b)]. We observe that the tetrahedral Li compound with the highest Li₂O content (eucryptite; distorted tetrahedra) has the highest BLD whereas the tetrahedral Li compound with the lowest Li₂O content (petalite; quasi-ideal tetrahedra) has the smallest BLD. Increased distortion shifts the position of the first peak to higher energy such that an increased distur-

tion may actually strengthen the Li–O bond or increase lithium's electron affinity. A possible explanation of the correlation between increased bond strength and site distortion could be charge compensation due to the proximity of Al (which is much higher in eucryptite than in petalite). The distortion of spodumene is much higher than for the tetrahedral minerals and we speculate that octahedral lithium sites may have their own distortion trend though more minerals would be needed in order to verify this claim. Outliers are also possible as shown in the calculation of the quadratic elongation for Mg-bearing minerals presented by Trcera *et al.* (2009).

5. Conclusions

The Li *K*-edge XANES spectra of a variety of compounds and minerals have been reported. The absorption edge is mainly due to $s \rightarrow p$ transitions leading to triply degenerate p -like states as was shown for LiF (Pascal *et al.*, 2014). Lithium sulfate also shows a sharp absorption edge which has been shown to be caused by triply degenerate p -like states reminiscent of LiF (Pascal *et al.*, 2014). Lithium carbonate shows a strong pre-edge which has been noted by Tsuji *et al.* (2002) as an indication of occupancy in the $2p$ orbital as is the case for Li₂O and Li metal. Additionally, the edge feature in Li₂CO₃ is very similar to the edge in the C *K*-edge spectrum which is typically associated with the π^* states (Fister *et al.*, 2011). Thus, the relative intensities and positions of the edge features can be used to estimate the covalency of the bond in question in other lithium compounds and minerals. The edge position of the lithium metasilicate, montebasite and lithium sulfate (Si, P and S, respectively) increases in energy with increasing electronegativity of the next nearest neighbour similar to the trend observed in the lithium halides (Handa *et al.*, 2005).

The lithium aluminosilicates were used to compare the Li site distortion with the edge energy and show how these factors changed with increasing lithium content. We demonstrate that, with higher distortion, lithium appears to have a higher electron affinity. Perhaps this can be explained by the role lithium must play in charge compensation when proximal to AlO₄ tetrahedra in eucryptite.

Lithium *K*-edge XANES measurements are useful for studying the bonding environment of lithium in a variety of different chemical compounds. Combining the experimental data with new numerical simulations on minerals, especially their density of states, would immensely improve our understanding of the XANES spectra. Investigating other edges within these systems (*e.g.* Si *L*-edge and O *K*-edge) would be valuable for corroborating the interpretations from the Li *K*-edge. Finally, it will be interesting to compare this information with future spectra of lithium silicate glasses.

Acknowledgements

The research described in this paper was performed at the Canadian Light Source, which is supported by the Canada Foundation for Innovation, Natural Sciences and Engineering Research Council of Canada, the University of Saskatchewan,

the Government of Saskatchewan, Western Economic Diversification Canada, the National Research Council Canada, and the Canadian Institutes of Health Research. A special thanks to Jean-Claude Boulliard, curator of the mineralogical collection of Université Pierre and Marie Curie, who provided all the mineral samples. GSH acknowledges funding from NSERC in the form of a discovery grant. Additionally we would like to thank two anonymous reviewers for their helpful comments.

Funding information

Funding for this research was provided by: Natural Sciences and Engineering Research Council of Canada (grant to Grant Henderson), Canada Foundation for Innovation, University of Saskatchewan, Canadian Institutes of Health Research, and Western Economic Diversification Canada.

References

- Albright, J. G. (1933). *Z. Kristallogr.* **84**, 1158–1167.
- Arlt, T. & Angel, R. J. (2000). *Phys. Chem. Miner.* **27**, 719–731.
- Baur, W. H. (1959). *Acta Cryst.* **12**, 988–994.
- Cannilo, E., Mazzi, F. & Rossi, G. (1966). *Acta Cryst.* **21**, 200–208.
- Clark, J. R., Appleman, D. E. & Papike, J. J. (1968). *Contr. Miner. Petrol.* **20**, 81–85.
- Daniels, P. & Fyfe, C. A. (2001). *Am. Mineral.* **86**, 279–283.
- Donnay, G. & Barton, R. J. (1972). *TMPM Tschermaks Petr. Mitt.* **18**, 273–286.
- Farges, F., Brown, G. E. J. & Rehr, J. J. (1996). *Geochim. Cosmochim. Acta*, **60**, 3023–3038.
- Fister, T. T., Schmidt, M., Fenter, P., Johnson, C. S., Slater, M. D., Chan, M. K. Y. & Shirley, E. L. (2011). *J. Chem. Phys.* **135**, 224513.
- Garvie, L. A. & Buseck, P. R. (2004). *Am. Mineral.* **89**, 485–491.
- Gatta, G. D., Danisi, R. M., Adamo, I., Meven, M. & Diella, V. (2012). *Phys. Chem. Miner.* **39**, 577–588.
- Geller, S. & Durand, J. L. (1960). *Acta Cryst.* **13**, 325–331.
- Groat, L. A., Chakoumakos, B. C., Brouwer, D. H., Hoffman, C. M., Fyfe, C. A., Morell, H. & Schultz, A. J. (2003). *Am. Mineral.* **88**, 195–210.
- Guggenheim, S. (1981). *Am. Mineral.* **66**, 1221–1232.
- Guggenheim, S. & Bailey, S. W. (1977). *Am. Mineral.* **62**, 1158–1167.
- Handa, K., Kojima, K., Taniguchi, K., Ozutsumi, K. & Ikeda, S. (2005). *Memoires of the SR Center Ritsumeikan University*, **7**, 3–6.
- Hatert, F., Ottolini, L., Wouters, J. & Fontan, F. (2012). *Can. Mineral.* **50**, 843–854.
- Hawthorne, F. C. & Henrys, D. J. (1999). *Eur. J. Mineral.* **11**, 201–216.
- Henderson, G. S., de Groot, F. M. F. & Moulton, B. J. A. (2014). *Rev. Mineral. Geochem.* **78**, 75–138.
- Hesse, K.-F. (1977). *Acta Cryst.* **B33**, 901–902.
- Hesse, K.-F. (1985). *Z. Kristallogr.* **172**, 147–151.
- Hu, Y. F., Zuin, L., Wright, G., Igarashi, R., McKibben, M., Wilson, T., Chen, S. Y., Johnson, T., Maxwell, D., Yates, B. W., Sham, T. K. & Reininger, R. (2007). *Rev. Sci. Instrum.* **78**, 083109.
- Jambon, A. & Semet, M. P. (1978). *Earth Planet. Sci. Lett.* **37**, 445–450.
- Jiang, N. & Spence, J. C. H. (2004). *Phys. Rev. B*, **69**, 115112.
- Jiang, N. & Spence, J. C. (2006). *Ultramicroscopy*, **106**, 215–219.
- Kasrai, M., Fleet, M. E., Bancroft, G. M., Tan, K. H. & Chen, J. M. (1991). *Phys. Rev. B*, **43**, 1763–1772.
- Kasrai, M., Yin, Z., Bancroft, G. M. & Tan, K. H. (1993). *J. Vac. Sci. Technol.* **11**, 2694–2699.
- Kikas, A., Nömmiste, E., Ruus, R., Saar, A. & Martinson, I. (2001). *Phys. Rev. B*, **64**, 235120.
- Kikkawa, J., Terada, S., Gunji, A., Haruta, M., Nagai, T., Kurashima, K. & Kimoto, K. (2014). *Appl. Phys. Lett.* **104**, 114105.
- Kobayashi, H., Emura, S., Arachi, Y. & Tatsumi, K. (2007). *J. Power Sources*, **174**, 774–778.
- Kogure, T. & Bunno, M. (2004). *Am. Mineral.* **89**, 1680–1684.
- Laan, G. van der (1991). *J. Phys. Condens. Matter*, **3**, 7443–7454.
- Lafuente, B., Downs, R. T., Yang, H. & Stone, N. (2015). *Highlights in Mineralogical Crystallography*, edited by T. Ambruster & R. M. Danisi, pp. 1–30. Berlin: W. de Gruyter.
- Lee, S. K., Eng, P. J. & Mao, H. (2014). *Rev. Mineral. Geochem.* **78**, 139–174.
- Li, C.-T. & Peacor, D. R. (1968). *Z. Kristallogr.* **126**, 46–65.
- Liebau, F. (1961). *Acta Cryst.* **14**, 399–406.
- London, D. (2005). *Lithos*, **80**, 281–303.
- Lu, Y.-C., Kwabi, D. G., Yao, K. P. C., Harding, J. R., Zhou, J., Zuin, L. & Shao-Horn, Y. (2011). *Energ. Environ. Sci.* **4**, 2999.
- Mauchamp, V., Boucher, F., Ouvrard, G. & Moreau, P. (2006). *Phys. Rev. B*, **74**, 115106.
- Mauchamp, V., Moreau, P., Ouvrard, G. & Boucher, F. (2008). *Phys. Rev. B*, **77**, 045117.
- Mottana, A., Marcelli, A., Cibin, G. & Dyar, D. M. (2002). *Rev. Mineral. Geochem.* **46**, 371–412.
- Moulton, B. J., Henderson, G. S., Sonnevile, C., O’Shaughnessy, C., Zuin, L., Regier, T. & de Ligny, D. (2016). *Chem. Geol.* **420**, 213–230.
- Neuville, D. R., Cormier, L., Flank, A.-M., Prado, R. J. & Lagarde, P. (2004). *Eur. J. Mineral.* **16**, 809–816.
- Ogasawara, Y. et al. (2015). *J. Power Sources*, **287**, 220–225.
- Olovsson, W., Tanaka, I., Mizoguchi, T., Puschnig, P. & Ambrosch-Draxl, C. (2009a). *Phys. Rev. B*, **79**, 041102.
- Olovsson, W., Tanaka, I., Puschnig, P. & Ambrosch-Draxl, C. (2009b). *J. Phys. Condens. Matter*, **21**, 104205.
- Pascal, T. A., Boesenberg, U., Kostecki, R., Richardson, T. J., Weng, T.-C., Sokaras, D., Nordlund, D., McDermott, E., Moewes, A., Cabana, J. & Prendergast, D. (2014). *J. Chem. Phys.* **140**, 034107.
- Prado, R. J. & Flank, A.-M. (2005). *Phys. Scr.* **T115**, 165–167.
- Rieder, M. (1968). *Science*, **160**, 1338–1340.
- Ross, N. L., Zhao, J., Slebodnick, C., Spencer, E. C. & Chakoumakos, B. C. (2015). *Am. Mineral.* **100**, 714–721.
- Roy, R. & Osborn, E. F. (1949). *Contribution from School of Mineral Industries, The Pennsylvania State College*, **71**, 2086–2095.
- Sartori, F., Franzini, M. & Merlino, S. (1973). *Acta Cryst.* **B29**, 573–578.
- Taguchi, N., Kitta, M., Sakaebe, H., Kohyama, M. & Akita, T. (2015). *J. Electron Spectrosc. Relat. Phenom.* **203**, 40–44.
- Tomascak, P. B. (2004). *Rev. Mineral. Geochem.* **55**, 153–195.
- Trcera, N., Cabaret, D., Rossano, S., Farges, F., Flank, A.-M. & Lagarde, P. (2009). *Phys. Chem. Miner.* **36**, 241–257.
- Tsuji, J., Nakamatsu, H., Mukoyama, T., Kojima, K., Ikeda, S. & Taniguchi, K. (2002). *X-ray Spectrom.* **31**, 319–326.
- Wang, D. & Zuin, L. (2017). *J. Power Sources*, **337**, 100–109.
- Waychunas, G. A. (1987). *Am. Mineral.* **72**, 89–101.
- Wenger, M. & Ambruster, T. (1991). *Eur. J. Mineral.* **3**, 387–400.
- Wyckoff, R. W. G. (1963). *Cryst. Struct.* **1**, 85–237.
- Yiu, Y. M., Yang, S., Wang, D., Sun, X. & Sham, T. K. (2013). *J. Phys. Conf. Ser.* **430**, 012014.
- Zemann, J. (1957). *Acta Cryst.* **10**, 664–666.